IOPscience iopscience.iop.org

Hemispherical wineglass resonators fabricated from the microcrystalline diamond

This content has been downloaded from IOPscience. Please scroll down to see the full text.

View the table of contents for this issue, or go to the journal homepage for more

Download details:

IP Address: 169.237.108.201
This content was downloaded on 27/11/2013 at 04:12

Please note that terms and conditions apply.

2013 J. Micromech. Microeng. 23 125016

IOP PUBLISHING JOURNAL OF MICROMECHANICS AND MICROENGINEERING

J. Micromech. Microeng. **23** (2013) 125016 (8pp) doi:10.1088/0960-1317/23/12/125016

Hemispherical wineglass resonators fabricated from the microcrystalline diamond

Amir Heidari[1], Mei-Lin Chan[1], Hsueh-An Yang[2], Gerardo Jaramillo[1], Parsa Taheri-Tehrani[1], Peter Fonda[1], Hadi Najar[1], Kazuo Yamazaki[1,2], Liwei Lin[2] and David A Horsley[1]

[1] Department of Mechanical and Aerospace Engineering, University of California Davis, California, 95616, USA

[2] Department of Mechanical Engineering, University of California Berkeley, California, USA

E-mail: dahorsley@ucdavis.edu

Received 15 July 2013, in final form 3 October 2013
Published 11 November 2013
Online at stacks.iop.org/JMM/23/125016

Abstract

We present the development of millimeter scale 3D hemispherical shell resonators fabricated from the polycrystalline diamond, a material with low thermoelastic damping and very high stiffness. These hemispherical wineglass resonators with 1.1 mm diameter are fabricated through a combination of micro-electro discharge machining (EDM) and silicon micromachining techniques. Using piezoelectric and electrostatic excitation and optical vibration measurement, the elliptical wineglass vibration mode is determined to be at 18.321 kHz, with the two degenerate wineglass modes having a relative frequency mismatch of 0.03%. A study on the effect of the size and misalignment of the anchor and resonator's radius variation on both the average frequency and frequency mismatch of the 2θ elliptical vibration modes is carried out. It is shown that the absolute frequency of a wineglass resonator will increase with the anchor size. It is also demonstrated that the fourth harmonic of radius variation is linearly related to the frequency mismatch.

(Some figures may appear in colour only in the online journal)

1. Introduction

The commercial hemispherical resonator gyroscope (HRG) is a high-precision and highly reliable solid-state gyroscope that achieves inertial grade performance [1, 2]. The topology of an axisymmetric hemispherical shell mounted on a stem minimizes the unwanted coupling of the hemispherical resonator's vibration to the base substrate and along with the use of high-purity fused-quartz materials, results in the high mechanical quality factor, Q. The HRG is one of the few vibratory gyroscopes that can be operated as a rate-integrating gyroscope (RIG) which produces a voltage output proportional to the rotation angle rather than the angular rotation rate [3–5].

These characteristics have spurred the recent interest in the development of microscale HRGs that can be mass manufactured at a wafer scale to achieve low-cost inertial grade sensors with the small volume and large dynamic range. In principle, achieving a millimeter scale RIG presents many challenges due to the resonator's Coriolis-coupled the two degenerate vibration modes used for rotation sensing. These two modes must be closely matched in resonant frequency and have high Q since any frequency mismatch becomes indistinguishable and can generate a bias error [6, 7]. For example, a 1 Hz frequency mismatch between these modes produces a bias error of 360 $^\circ$ s^{-1}, a figure many orders of magnitude larger than the bias instability of a typical commercial MEMS rate gyroscope today.

To achieve mode-matching and high Q performance in a hemispherical resonator, geometric uniformity and symmetry in combination with a low thermoelastic damping structural material are critical. Materials such as polysilicon [8, 9], silicon nitride [4], and glass [10] have been used as the structural material for these resonators, and many different methods

 © 2013 IOP Publishing Ltd Printed in the UK & the USA

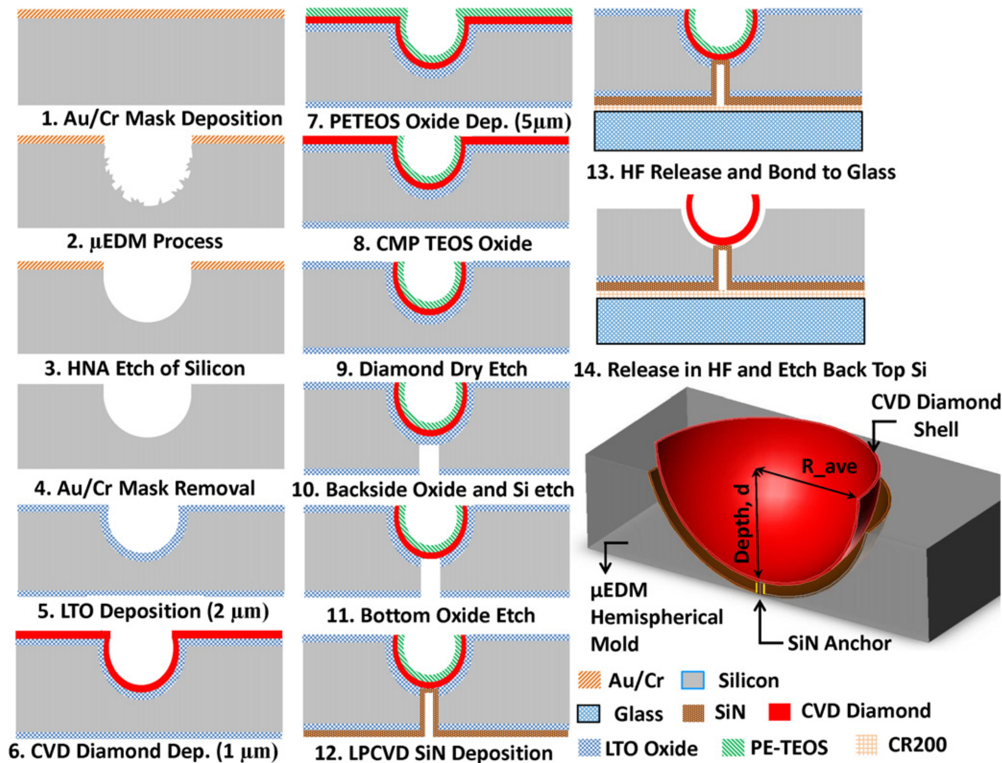

Figure 1. A fabrication process flow for creating CVD diamond hemispherical shell resonators.

have been employed to create these hemispherical structures, including wafer-scale glass blowing [11], bulk silicon etching [9, 12] and a combination of precision machining and bulk etching [13, 14].

In this work, we describe the development and characterization of millimeter scale 3D hemispherical wineglass resonators made from the microcrystalline diamond (MCD). MCD is used as the structural material due to its unique material properties such as high stiffness and low thermoelastic damping [15–18]. Thin-film polycrystalline diamond offers the enhanced mechanical properties, including significantly higher stiffness, strength, hardness, thermal conductivity, and chemical robustness, versus silicon and most other thin-film materials commonly used in microfabrication technologies. The excellent strength to the density ratio and diamond's superior surface properties make this an ideal material for low surface losses and ultra-low thermoelastic damping, both significant properties required for a resonator.

A novel fabrication method based on micro-electro discharge machining (EDM) [19] is employed to fabricate hemispherical silicon molds that are used to form 1.1 mm diameter diamond wineglass resonators with Si_3N_4 anchors. These resonators are released by dissolving the silicon mold wafer; and their frequency response is characterized using vibratory excitation and optical detection. The effect of geometric variations (e.g. resonator's radius, anchor size, and centering of the anchor) on both the average frequency ($\bar{f}$) and frequency mismatch (Δf) of the 2θ elliptical vibration modes is studied using both FEM and experimentation.

2. Fabrication

Resonators are fabricated through a combination of micro-EDM and silicon micromachining techniques (figure 1). A low resistivity (0.008–0.2 Ω cm), silicon substrate with standard thickness (500 ± 25 μm) is first deposited with a metal hard mask. The 1.1 mm diameter hemispherical silicon mold is then formed via EDM, after which an HNA (HF/nitric/acetic acid with 2:3:3 volume ratio concentration) etch chemically polishes the inside surface of the machined hemispherical mold for 120 s, while a metal hard mask (30 nm Ti/120 nm Au) protects the top surface of the silicon substrate. Image analysis was used to demonstrate that the finished silicon mold exhibits high symmetry, having a radial standard deviation below 6 μm for a 500 μm radius shell [12] and a surface roughness of 4 nm measured at the inside of the silicon mold.

After stripping the etch mask, a 2 μm thick SiO_2 sacrificial layer is conformally deposited on the silicon mold via chemical vapor deposition (CVD). The SiO_2 surface is then seeded using an ultrasonic seeding suspension containing the nanocrystalline diamond powder with diameter from 5–50 nm dispersed in the solvent. Using a methane (CH_4) concentration of 1.5% and a relative tetramethyl boron/CH_4 concentration of 444 ppm, a 1 μm thick boron-doped diamond structural layer is deposited via hot-filament chemical vapor deposition (HFCVD, sp^3 Diamond Technologies). A 5 μm thick plasma enhanced tetraethyl-orthosilicate (PE-TEOS) oxide layer is deposited to mask the topside of the wafer. PE-TEOS is selected to ensure the conformal oxide mask coverage on the rough MCD surface. Chemical mechanical polishing (CMP) removes the oxide mask at the rate of ∼ 300 nm min^{-1} from the wafer surface, but retains the mask within the mold.

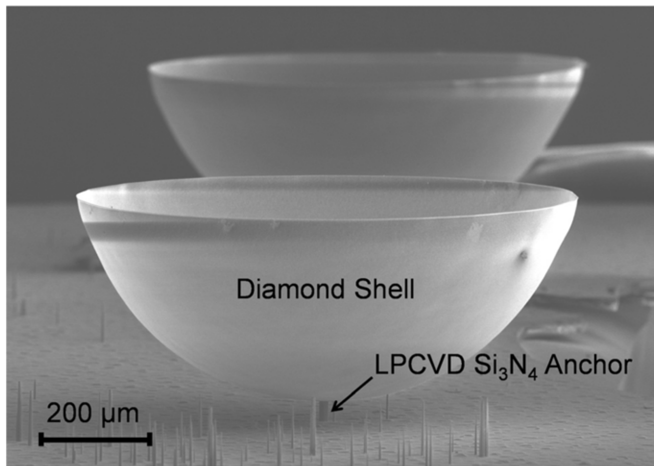

Figure 2. SEM micrograph shows an array of totally released diamond shells attached to the silicon substrate with LPCVD Si_3N_4 anchors.

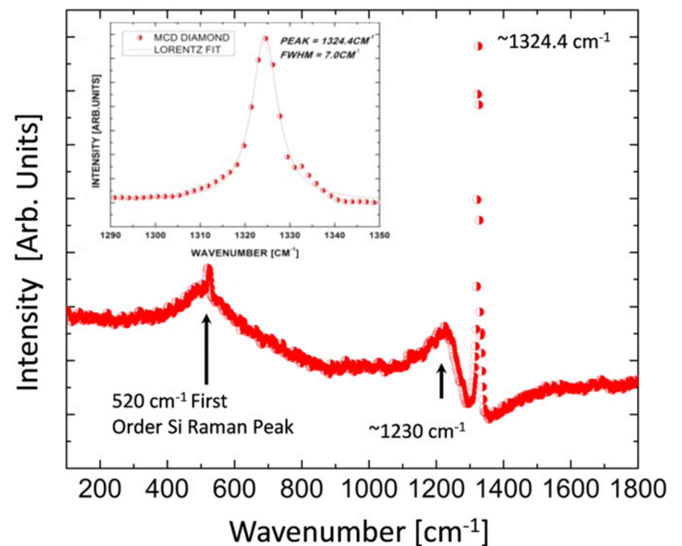

Figure 3. Raman spectrum of boron-doped microcrystalline diamond. Figure inset shows the Lorentzian fit for the first-order Raman peak for the sp^3 diamond.

The exposed diamond on the wafer surface is etched in an O_2/CF_4 plasma at a flow ratio of 50:1 in an inductively coupled plasma (ICP) etcher (SPTS Inc., APS etcher) at a process pressure of 30 m Torr, leaving diamond only within the hemispherical molds. The wineglass anchors are formed by opening lithographically-defined holes on the back of the wafer using the plasma etching of Si and SiO_2, after which the holes are refilled with LPCVD Si_3N_4. Finally, the diamond shells are released in 49% hydrofluoric acid (HF) to remove the sacrificial SiO_2, after which the silicon mold is either partially or completely removed to facilitate the non-contact optical characterization of the resonator. In order to etch back the silicon from the top of the die, either XeF_2 or silicon wet etch (HNA) is used in these experiments. For the latter method, the HNA with the above-mentioned volumetric concentration (2:3:3) takes $\sim$ 1 h to etch back the 500 $\pm$ 25 μm silicon. Since the LPCVD Si_3N_4 protects the die backside, the HNA starts to attack the top and the edges of die. SEM micrographs in figure 2 show an array of totally released diamond shells attached to the silicon substrate with LPCVD Si_3N_4 anchors. The columnar spires shown in the image are composed of Si_3N_4 and result from defects in the backside silicon etch that result in Si_3N_4-filled holes in the silicon wafer. When the wafer is etched away, these Si_3N_4 spires remain along with the diamond hemispheres.

Through the control of the HFCVD deposition conditions, either micro-crystalline diamond (MCD) or nano-crystalline diamond (NCD) films can be deposited. Here, MCD was selected as the structural material, a choice motivated by the higher sp^3 content of MCD films and reduced density of grain boundaries; both properties translate into high Q-factors of 71 400 at 299.86 MHz for a diamond disc resonator [20] and 81 646 at 473.3 kHz for a diamond double ended tuning fork [15].

In order to inspect the quality of the diamond film, Raman spectroscopy was used. This technique relies on the inelastic scattering of the monochromatic light—typically a laser. Once the sample is irradiated with the laser source, the laser interacts with molecular vibrations, phonons or other excitations in the system and shifts up or down the energy of the laser photons [21]. This technique gives one the ability to inspect and observe the quality of the diamond films such as the sp^3 contents. The Raman spectrum obtained for the boron-doped MCD film using a 514.5 nm excitation wavelength is shown in figure 3. In the sp^3 single crystal diamond, the dominant feature of the Raman spectrum is the first-order line at 1332 cm^{-1}. In our measurement, this peak is down-shifted to 1324.4 cm^{-1} and has full-width at half-maximum = 7.0 cm^{-1}, consistent with previous studies on the effects of the residual stress and boron doping in the MCD films [22]. The smaller peak observed at 520 cm^{-1} corresponds to the first-order Raman line for Si and the other peak at 1230 cm^{-1} is also broadly consistent with the peaks in the phonon density of states (PDOS) of diamond and is attributed to the incorporation of boron in the diamond lattice [23]. The comparison between the diamond and non-diamond components (at 1500–1550 cm^{-1}), quantified by the intensity ratio I(1332 cm^{-1})/I(1500 cm^{-1}) shows the high fraction of the sp^3 content and purity of the diamond film used in the hemispherical resonator structure.

In order to study the effect of the residual stress on the resonance frequency of the resonator, a FEM simulation is carried out. After applying of 200 MPa residual stress in the radial direction of the shell resonator in the FEM model and running a nonlinear analysis, the resonance frequency has shifted 2–3%. The main reason of this small change in frequency due to residual stress is the high elastic's modulus of MCD (up to seven times of silicon). Consequently, we have neglected the effect of the residual stress in our future analyses.

The SEM view of the MCD shell resonator shown in figure 4(*a*) illustrates the highly faceted surface of the MCD layer, which has a grain size in the range between 0.2 and 0.5 μm. The surface roughness of the resonator is dominated by the roughness of the MCD film, which was observed to increase with increasing MCD film thickness. Figure 4(*b*) shows part of a cracked shell to illustrate the columnar nature of

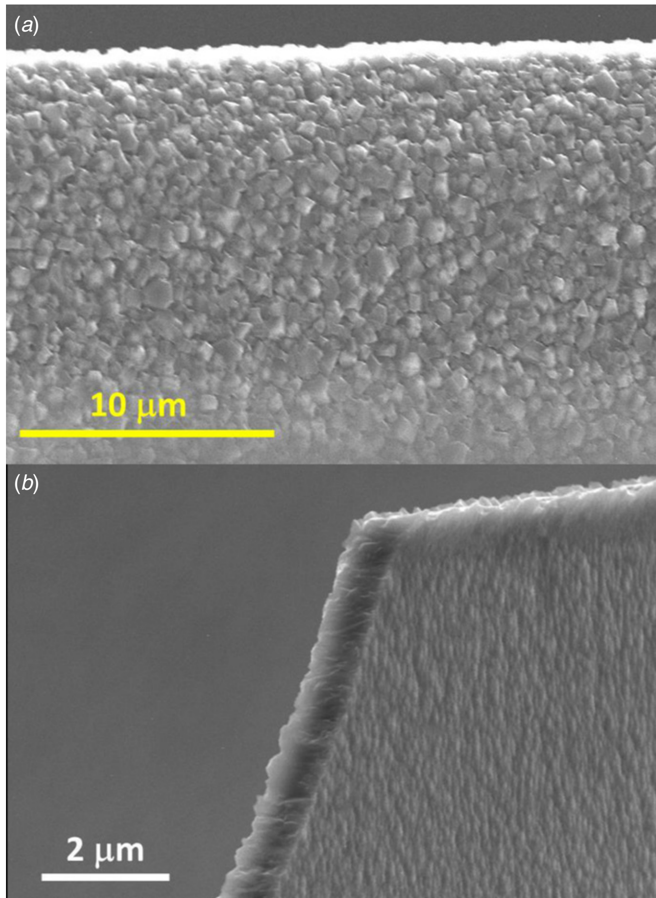

Figure 4. SEM micrographs of (*a*) a top view of the MCD film and (*b*) a representative sample diamond shell with a cracked rim to show the columnar nature of the MCD structural layer.

the diamond grains beginning from the nanocrystalline seeding layer on the SiO_2 surface of the mold wafer. The thickness of the diamond shell is between 0.8 and 1.0 μm.

3. Experiments

The vibration frequency response of diamond hemispherical resonators was characterized using a Laser doppler vibrometer (LDV, Polytec Inc.) both in air and in vacuum. Figure 5(*a*) shows the schematic of the testing setup, where the diamond shell was mounted vertically onto a shear mode piezoelectric actuator (Noliac A/S) with a bandwidth of 1.7 MHz to excite the shell. The single point LDV laser spot was focused through a 10x microscope objective onto the rim of the shell to measure the radial displacement of the vibrating shell. A miniature rotation stage and two-axis goniometer (OptoSigma) were used to tune the incidence angle of the laser onto the shell for the maximum signal to a noise ratio. The whole setup was also mounted in a vacuum chamber to allow measurements at low pressures.

In an alternative measurement setup, shown in figure 5(*b*), shells were mounted on a glass slide and excited electrostatically using an amplified ac voltage ($V_{pp} \sim 25.4$ V) applied to a probe tip placed approximately 20 μm from the shell rim. Since the probe and shell resonator were in the horizontal plane, the vertical LDV laser beam was redirected to the horizontal plane using a 45° prism. The whole setup was also mounted in a vacuum probe station (MMR Technologies Inc.) to allow the measurement at sub-mPa pressures.

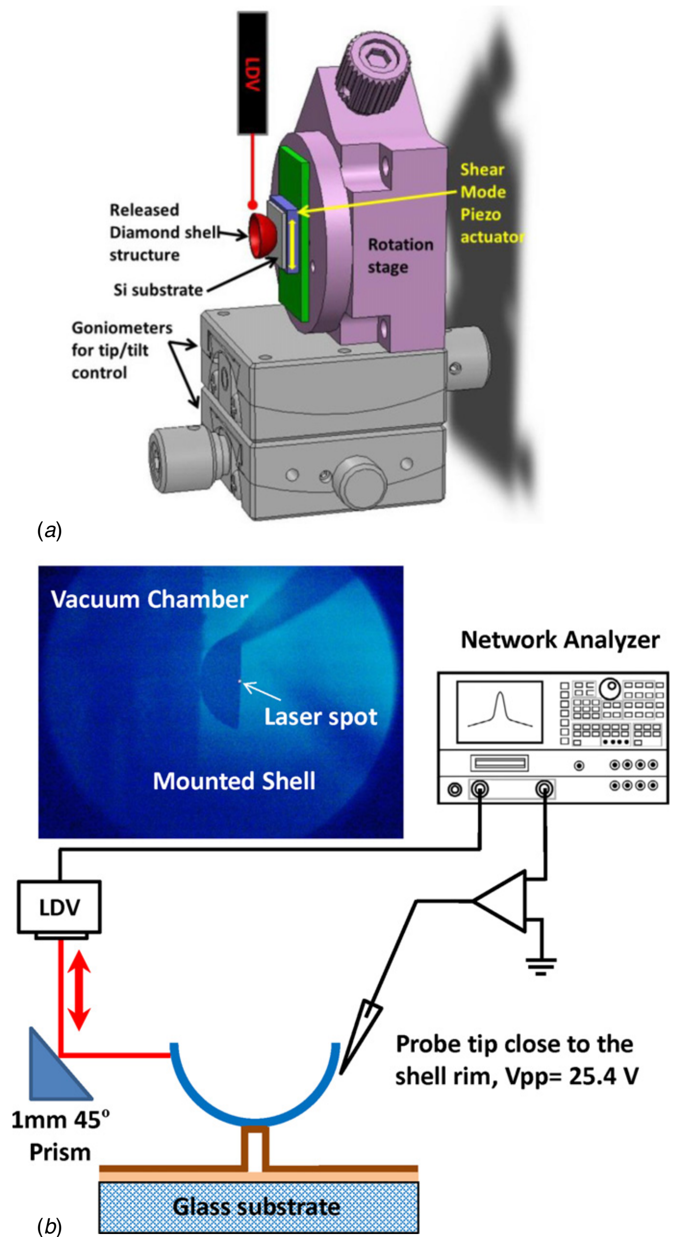

Figure 5. (*a*) Schematic of experimental setup used to characterize the diamond shell (rotation stage, piezoelectric actuator); (*b*) Setup used for the electrostatic excitation of a diamond shell using probes and the laser spot focused on the shell rim. The inset contains an image of the 1 mm shell, showing the laser spot and excitation probe.

The frequency response of a hemispherical shell in vacuum at 4.3 mPa is shown in figure 6. Resonance peaks at $f_1 = 18.316$ kHz and $f_2 = 18.321$ kHz, corresponding to the two 2θ elliptical vibration modes were observed. The frequency mismatch between these two degenerate resonance modes, was $\Delta f = 5$ Hz, or 0.03% when normalized by the average frequency $\bar{f} = (f_1 + f_2)/2$. This frequency mismatch is obtained from few resonators, but the frequency mismatch of other tested resonators ranged up to 500 Hz. The observed Q

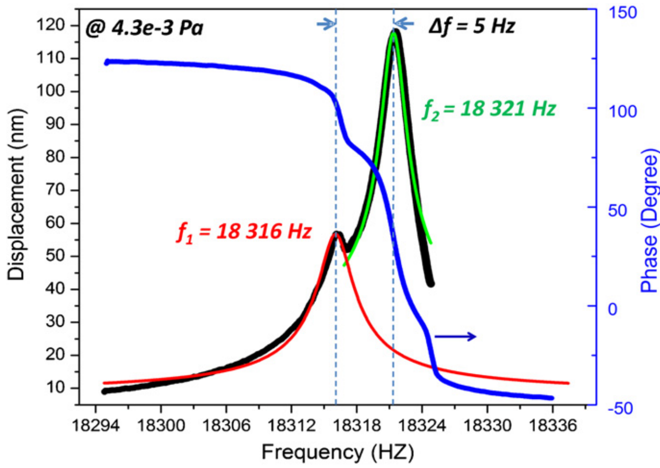

Figure 6. A measured frequency response showing the 2θ elliptical modes; $\Delta f = 5$ Hz at 18.316 kHz in 4.3 mPa vacuum ($\Delta f/\bar{f} = 0.03\%$).

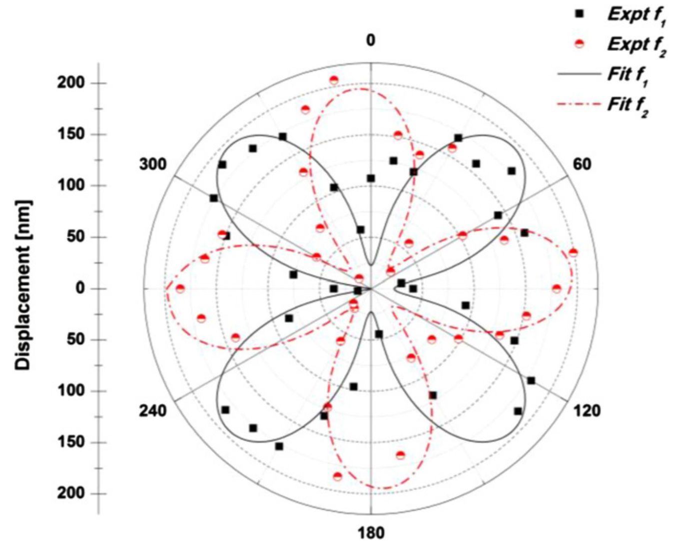

Figure 7. Measured displacement amplitude along the rim of the resonator shell with excitation at f_1 (■) and f_2 (●) illustrating the expected elliptical mode shapes.

was approximately 10 000 for degenerate 2θ vibration modes and 20 000 for 3θ vibration modes.

The elliptical mode shapes at frequencies f_1 and f_2 were identified by measuring the radial vibration around the perimeter of the shell, as the shell is rotated through 360°. At every 10° interval, the frequency response of the structure is measured and the displacement at f_1 and f_2 is extracted. Figure 7 shows the polar plot of the shell displacement as it is excited at each frequency. Each measured mode shape exhibits the four nodes which are characteristic of the elliptical modes. By employing a fitting function described by $|A_i \sin(2\theta + \phi_i)|$, the angle between the principal axes of elasticity is extracted to be ~45° in good agreement with theory.

4. Sources of frequency mismatch

Experimental and finite element method (FEM) studies were conducted to evaluate the impact of variations in the anchor size, anchor misalignment, and resonator diameter on the frequency and frequency mismatch of the elliptical vibration modes.

4.1. Effect of anchor size, symmetry and misalignment

A set of FEM simulations in COMSOL™ Multiphysics were carried out to estimate the effect of the anchor size on the absolute frequency and frequency mismatch of the shell resonator. Young's modulus (E), Poisson's ratio (υ) and the density (ρ) of the MCD were considered to be 800 MPa, 0.25, and 3515 Kg m^{-3}, respectively, in accordance with values measured using cantilever beams [15]. FEM studies were first conducted based on an ideal symmetric resonator in which the frequencies of the two degenerate 2θ vibration modes are equal ($f_1 = f_2 = \bar{f}$). The analytical formula for the frequency of the $n\theta$ vibration mode is given by [24]:

$$\bar{f} = \frac{1}{2\pi}\left[\frac{n(n^2-1)}{R^2}\right]\sqrt{\frac{EI_{n1}t^2}{3(1+\upsilon)\rho J_{n1}}}, \quad n = 2, 3, 4\ldots, \quad (1)$$

where t and R are the thickness and radius of the hemispherical shell; I_{n1} and J_{n1} are the dimensionless parameters that depend on the angular extent of the shell [24]. Here, the shell is a hemisphere extending $\pi/2$ radians from the center anchor and for the $n = 2$ mode I_{n1} and J_{n1} are 0.292 and 1.53, respectively.

For a wineglass resonator with the diameter of 1 mm, thickness of 1 μm, equation (1) predicts $\bar{f} = 13.78$ kHz. Since the analytical formula does not account for the anchor at the base of the resonator, FEM analysis was used to find the frequency at different anchor sizes (figure 8). As shown, the frequency increases linearly with the anchor diameter and adding a 20 μm diameter anchor increases $\bar{f}$ by 25% to 17.26 kHz.

The effect of the anchor size on the average frequency $\bar{f}$ and frequency mismatch Δf was also experimentally studied. The first fabrication run was carried out by using a silicon anchor whose diameter was controlled by using a XeF_2 timed-etch. As shown in SEM images in figure 8(*a*), the anchors resulting from this process were large (~200 μm) which resulted in high $\bar{f}$ and Δf. In the next fabrication run, the hemispheres were mounted on a glass substrate using a poly (methyl methacrylate) (PMMA) layer in figure 8(*b*). The rest of the shells were fabricated using the process flow shown in figure 1 and had LPCVD silicon nitride anchors. Depending on the duration of the release etch; residual silicon remained around the anchor, resulting in resonators with anchor diameters varying from 20 to 120 μm. The values for $\bar{f}$ observed in experiments follow the same trend observed in FEM simulations. However, Δf essentially depended on the shell symmetry and the similar trend observed here are not related to the anchor size but are instead due to the improved symmetry of the anchor and resonator itself.

The frequency mismatch resulting from the anchor misalignment from the shell center is shown in figure 9 for wineglasses with 0.5 and 1 μm wall thickness, the diameter of 1 mm and the thickness of 1 μm. Based on the simulation results, the anchor misalignment does not have a significant

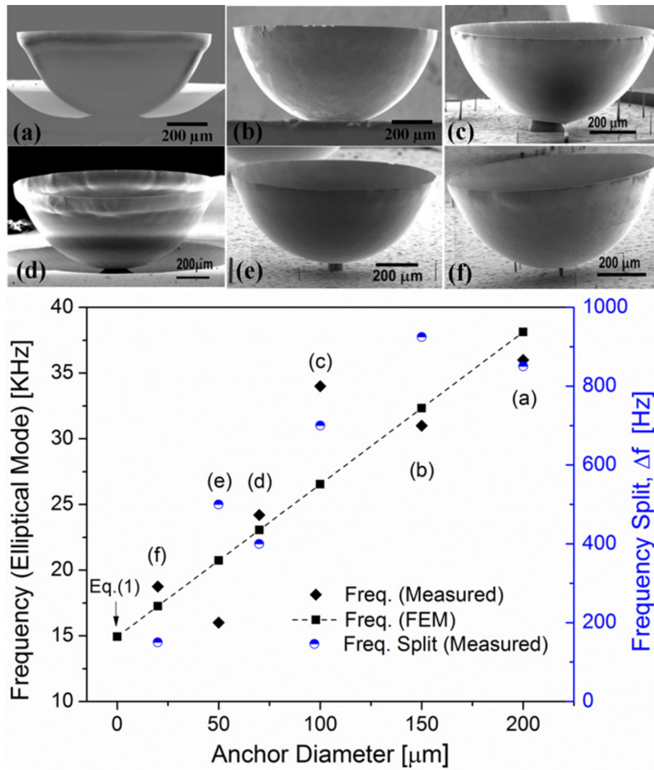

Figure 8. The SEM images of the diamond shell with different anchor diameter sizes (*a*)–(*f*); and simulation and experimental results of the effect of the anchor diameter on the average frequency. The trend observed in the frequency mismatch Δf is not due to the anchor size.

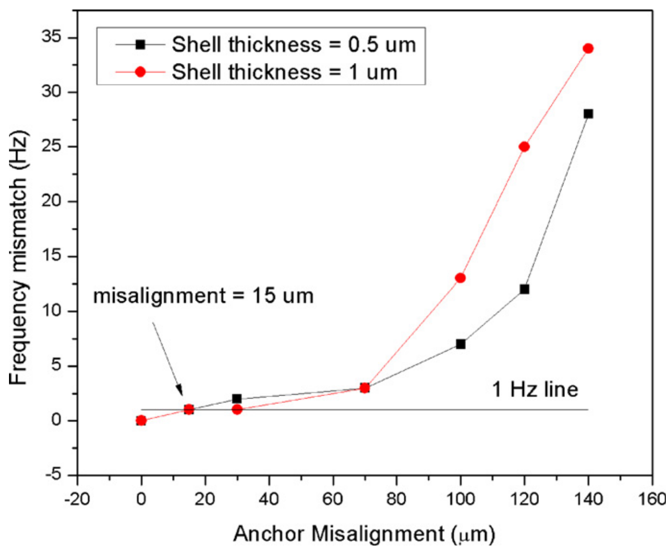

Figure 9. The effect of the anchor misalignment on the frequency mismatch (Δf) of the 2θ elliptical vibration modes of a shell.

effect on the frequency mismatch (Δf) if the misalignment is less than 15 μm ($\Delta f = 1$ Hz). This misalignment can be managed in most lithography processes.

4.2. Effect of wineglass radius variations

An approach based on Fourier analysis and originally applied to ring gyros [25] was used to study the impact of variations

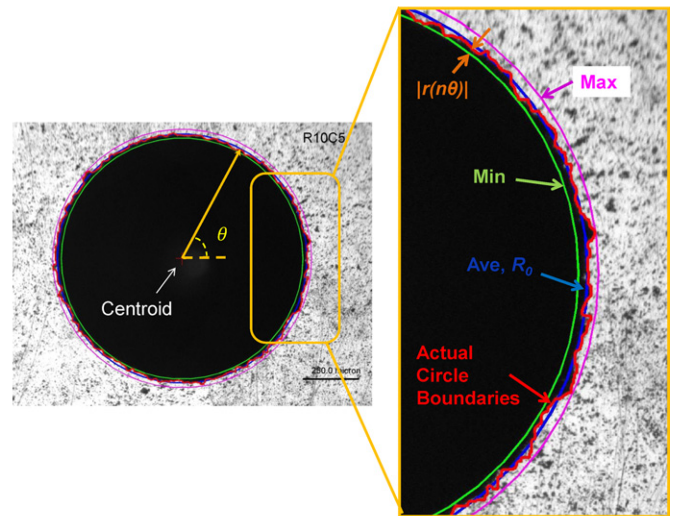

Figure 10. The quantitative evaluation of the EDM silicon mold edge profile.

in the wineglass radius on the frequency mismatch. The radial profile of each wineglass as a function of angle, $R(\theta)$ was extracted from the images of machined silicon molds used for the fabrication of hemispherical resonators (step 4, figure 1). Image acquisition was carried out using a microscope with a 5x objective (Mitutoyo M Plan APO). A Matlab^{TM} image processing code was developed to process the individual images and extract the quantitative measurements of the finished features. Figure 10 shows an optical image, where the zigzag curve traces the actual rim and the middle, inner and outer lines show circles corresponding to the average, minimum and maximum radius of the mold, respectively.

Using Fourier series, it is possible to model the closed circle curve by the single-valued curves as follows:

$$R(\theta) = R_0 + \sum_{n=1}^{N} r_c \cos(n\theta) + r_s \sin(n\theta), \tag{2}$$

where $R(\theta)$ denotes the silicon mold edge profile with respect to the angle θ (figure 10) and R_0, r_c and r_s are the Fourier coefficients. The particular case considered here in some detail is that where the profile is assumed to contain only a single harmonic variation. In this case, the silicon mold edge profile can be expressed quite generally as follows:

$$R(\theta) = R_0 + |r(n\theta)| \cos n\theta, \tag{3}$$

where $|r(n\theta)|$ is the amplitude of the profile variations measured from the mean radius R_0, and n is the harmonic number of the profile (figure 10). In ring gyros, it has been shown that fourth harmonic radial deviations $|r(4\theta)|$ ($n = 4$ in equation (3)), have the largest effect on the frequency mismatch of the 2θ elliptical modes [25–27]. FEM simulation (COMSOL^{TM} Multiphysics) was used to model the frequency mismatch of our 3D shell as a function of the amplitude of the fourth harmonic component, $|r(4\theta)|$. The 3D shell geometry used for FEM simulation was generated in SolidWorks beginning with a 2D circular profile with the desired $|r(4\theta)|$ deviation. Then, a quarter-circular arc-line was revolved along this 2D circular profile about a center axis

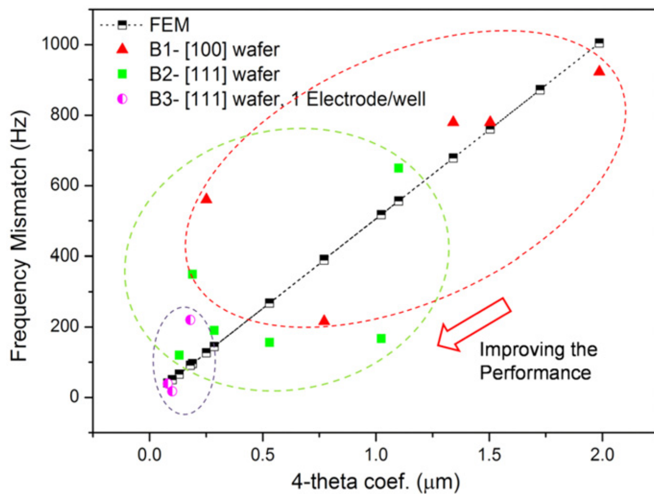

Figure 11. The measured and simulated frequency mismatch Δf versus the fourth harmonic of radius variation, $|r(4\theta)|$.

of rotation to produce a hemisphere with the desired radial variations. A 1 μm thickness was added to the generated shell surface and the final geometry was exported to COMSOL™ for FEM analysis. Simulation results, shown in figure 11, demonstrate a linear relationship between $|r(4\theta)|$ and the frequency mismatch.

To verify the simulation results, three batches of resonators were also fabricated using different processing conditions and silicon wafer crystalline orientations in order to realize different levels of radius variation. For the EDM processing conditions, a rough machining step was first conducted with adequate discharge energy to reduce the electrode wear (5 μs discharge time, 4 A current and 120 V electrode potential), followed by a finishing step which used lower discharge energy (0 μs discharge time, 1 A current and 90 V potential), in conjunction with the electrode orbital motion of 40 μm/side (EDM conditions are described in more detail in [14]). Batch 1 used ⟨100⟩ wafers, while batches 2 and 3 used ⟨111⟩ wafers. In batches 1 and 2, the same electrode was used to EDM all features on a given wafer, whereas in batch 3, a new electrode was used to machine each hemispherical mold. After the fabrication and testing of the shells from each batch, a good correlation between FEM and experimental results was achieved, showing that $|r(4\theta)| = 100$ nm results in $\Delta f = 17$ Hz in air, as shown in figure 11.

The main source for the higher $|r(4\theta)|$ deviations (and as a result, higher frequency mismatch) in the batch 1 resonators (B1 in figure 11) is that the ⟨100⟩ wafers are etched anisotropically by the post-EDM HNA polishing etch (step 3, figure 1). Using ⟨111⟩ wafers rather than ⟨100⟩ wafers in batch 2 eliminated this problem, and the remaining asymmetry is only related to the EDM process. Using one electrode per mold in batch 3 also improved the EDM process, improving the overall symmetry, reducing $|r(4\theta)|$ and reducing the frequency mismatch by more than a factor of 5 when compared to resonators from batch 2.

5. Conclusion

We developed microcrystalline diamond wineglass resonators, and demonstrated the vibration frequency response of these resonators. Using a combination of EDM and silicon micromachining technologies, hemispherical silicon molds were made, and microcrystalline diamond wineglass resonators were formed within these molds. These resonators were characterized using electrostatic excitation applied through a probe tip and optical detection at the rim of the shell to determine the natural frequencies and mode shapes of the 2θ elliptical vibration modes. In the best resonator, the elliptical modes were observed at $f_1 = 18.316$ kHz and $f_2 = 18.321$ kHz, showing a frequency mismatch $\Delta f/\bar{f} \sim 0.03\%$. The effect of the resonator radius, radius variation, and diameter and misalignment of the anchor, on both the average frequency and frequency mismatch of the 2θ elliptical vibration modes were studied through experimentation and FEM modeling. The experimental results show that the absolute frequency linearly increases with the increasing anchor diameter. The experimental results also show that the fourth harmonic of radius variation, $|r(4\theta)|$, is linearly related to the frequency mismatch of the resonator.

Acknowledgments

This work is supported by DARPA under grant W31P4Q-11-1-0003. The authors would like to thank the support of the staff in UC Davis Northern California Nanotechnology Center and UC Berkeley Marvell Nanolab.

References

[1] Lynch D D 1984 Hemispherical resonator gyro *IEEE Trans. Aerosp. Electron. Syst. AES* **20** 414–44

[2] Matthews A D and Bauer D A 1995 Hemispherical resonator gyro for precision pointing applications *Proc. SPIE the Int. Soc. for Optical Engineering, 2466 3rd Conf. on Space Guidance Control and Tracking II* pp 128–41

[3] Cho J, Gregory J A and Najafi K 2011 Single-crystal-silicon vibratory cylindrical rate integrating gyroscope (CING) *16th Int. Conf. Solid-State Sensors, Actuators and Microsystems (5–9 June, Beijing, China)* pp 2813–6

[4] Trusov A A, Prikhodko I P, Zotov S A, Schofield A R and Shkel A M 2010 Ultra-high Q silicon gyroscopes with interchangeable rate and whole angle modes of operation *IEEE Sensors (1–4 Nov., Kona, HI)* pp 864–7

[5] Loper E J, Lynch D D and Stevenson K M 1986 Projected performance of smaller hemispherical resonator gyros *PLANS'86: Position Location and Navigation Symp. (4–7 Nov., Las Vegas, NV)* pp 61–4

[6] Lynch D D 1995 Vibratory gyro analysis by the method of averaging *2nd Saint Petersburg Int. Conf. on Gyroscopic Technology and Navigation (San Petersburg, Russia)* pp 26–34

[7] Friedland B and Hutton M 1978 Theory and error analysis of vibrating-member gyroscope *IEEE Trans. Autom. Control* **23** 545–56

[8] Hwang C 1966 Some experiments on the vibration of a hemispherical shell *J. Appl. Mech.* **33** 817–24

[9] Sorenson L, Gao X and Ayazi F 2012 3D Micromachined hemispherical shell resonators with integrated capacitive

transducers *IEEE 25th Int. Symp. on Micro Electro Mechanical Systems (Paris, France)* pp 167–71

[10] Zotov S A, Trusov A A and Shkel A M 2012 Three-dimensional spherical shell resonator gyroscope fabricated using wafer-scale glassblowing *J. Microelectromech. Syst.* **21** 509–10

[11] Prikhodko I P, Zotov S A, Trusov A A and Shkel A M 2011 Microscale glass-blown three dimensional spherical shell resonators *J. Microelectromech. Syst.* **20** 691–701

[12] Fegely L C, Hutchison D N and Bhave S A 2011 Isotropic etching of 111 SCS for wafer scale manufacturing of perfectly hemispherical silicon molds *Transducers'11: 16th Int. Conf. on Solid-State Sensors, Actuators and Microsystems (Beijing, China)* pp 2295–8

[13] Visvanathan K, Tao L and Gianchandani Y B 2011 3D-soule: a fabrication process for large scale integration and micromachining of spherical structures *IEEE 24th Int. Symp. on Micro Electro Mechanical Systems (Cancun, Mexico)* pp 45–8

[14] Chan M L, Fonda P, Reyes C, Xie J, Najar H, Lin L, Yamazaki K and Horsley D A 2012 Micromachining 3D hemispherical features in silicon via micro-EDM *IEEE 25th Int. Symp. on Micro Electro Mechanical Systems (Paris, France)* pp 289–92

[15] Najar H, Heidari A, Chan M L, Yang H A, Lin L, Cahill D G and Horsley D A 2013 Microcrystalline diamond micromechanical resonators with quality factor limited by thermoelastic damping *J. Appl. Phys. Lett.* **102** 1–4

[16] Najar H, Chan M L and Horsley D A 2012 Impact of doping and microstructure on quality factor of CVD diamond micromechanical resonators *FCS'12: IEEE Int. Proc. of Frequency Control Symp. and the European Frequency and Time Forum (Baltimore, USA)* pp 1–5

[17] Sepulveda N, Aslam D M and Sullivan J P 2006 Polycrystalline diamond MEMS resonator technology for sensor applications *J. Diamond Relat. Mater.* **15** 398–403

[18] Sepulveda N, Jing L, Aslam D M and Sullivan J P 2008 High-performance polycrystalline diamond micro- and nanoresonators *J. Microelectromech. Syst.* **17** 473–82

[19] Fonda P, Nakamoto K, Heidari A, Yang H-A, Horsley D A, Lin L and Yamazaki K 2013 A study on the optimal fabrication method for micro-scale gyroscopes using a hybrid process consisting of electric discharge machining, chemical etching or micro-mechanical milling *CIRP Ann.—Manuf. Technol.* **63** 183–6

[20] Akgul M, Schneider R, Ren Z, Chandler G, Yeh V and Nguyen C T C 2011 Hot filament CVD conductive microcrystalline diamond for high Q, high acoustic velocity micromechanical resonators *FCS'11: Joint Conf. of the IEEE Int. Frequency Control and the European Frequency and Time Forum (2–5 May, San Francisco, USA)* pp 1–6

[21] Douglas A, Skoog F, Holler J and Crouch S R 2007 *Principles of Instrumental Analysis* 6th edn (Belmont, CA: ThomsonBrooks/Cole) p 1039 chapter 17

[22] Wang W L, Polo M C, Sanchez G, Cifre J and Esteve J 1996 Internal stress and strain in heavily boron-doped diamond films grown by microwave plasma and hot filament chemical vapor deposition *J. Appl. Phys.* **80** 1846–51

[23] Bernard M, Deneuville A and Muret P 2004 Non-destructive determination of the boron concentration of heavily doped metallic diamond thin films from Raman spectroscopy *J. Diamond Relat. Mater.* **13** 282–6

[24] Gao S and Wu J 2007 Theory and finite element analysis of HRG *ICMA'07: Proc. of IEEE Int. Conf. on Mechatronics and Automation (5–8 Aug., Harbin, China)* pp 2768–72

[25] Fox C H J 1999 A simple theory for the analysis and correction of frequency splitting in slightly imperfect rings *J. Sound Vib.* **142** 227–43

[26] Hwang R S, Fox C H J and McWilliam S 1999 Free vibrations of elliptical rings with circumferentially variable thickness *J. Sound Vib.* **228** 683–99

[27] Hwang R S, Fox C H J and McWilliam S 1999 The in-plane vibration of thin rings with in-plane profile variations: part I. General background and theoretical formulation *J. Sound Vib.* **220** 386–405